Corrosion Science 202 (2022) 110314

Contents lists available at ScienceDirect

Corrosion Science

journal homepage: www.elsevier.com/locate/corsci

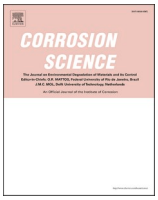

Effect of creep ageing on the corrosion behaviour of an Al–Cu–Li alloy

Bo Jiang [a,b,c], Chao Wang [a,b,c], Renguo Song [a,b,c], Shichen Li [d,*], Fuhua Cao [e,*], Danqing Yi [d]

[a] School of Materials Science and Engineering, Changzhou University, Changzhou, Jiangsu 213164, China
[b] Jiangsu Key Laboratory of Materials Surface Science and Technology, Changzhou University, Changzhou, Jiangsu 213164, China
[c] Jiangsu Collaborative Innovation Center of Photovolatic Science and Engineering, Changzhou University, Changzhou, Jiangsu 213164, China
[d] School of Materials Science and Engineering, Central South University, Changsha 410083, China
[e] State Key Laboratory of Nonlinear Mechanics, Institute of Mechanics, Chinese Academy of Sciences, Beijing 100190, China

ARTICLE INFO

Keywords:
Creep ageing
Al–Cu–Li alloy
Corrosion
Grain orientation

ABSTRACT

Creep ageing of Al–Cu–Li alloys induces precipitation of $T_1(Al_2CuLi)$ and a high fraction of low-angle grain boundaries (LAGBs) and dislocations in grain interior, factors potentially contributing to corrosion. Qualitative/quantitative analysis of precipitates and quasi-in-situ EBSD observations of stress free and stress added alloy reveal that fine dense precipitation of T_1 in grain interior and suppressed precipitation along grain/subgrain-boundary induced by stress adding make the corrosion mode evolve from intergranular to intragranular, and grain orientation displays as the most relevant metallurgical parameter for the localised corrosion although the fraction of LAGBs and dislocations have been greatly improved by stress loading.

1. Introduction

Creep ageing, which combines creep and age hardening processes, has been successfully applied to manufacturing parts that require machining, such as wings with severe dihedral angles, large contoured wing skins and wing panels [1–3]. Creep deformation during ageing has a significant impact on the precipitation and grain structure, which are important factors in the corrosion behaviour of the alloy [4–7].

During creep deformation, alloys suffer elastic or plastic deformation caused by point defects, line defects, planar defects or a mixture of these defects. Preferential nucleation and precipitation could be observed on these defects. In newly developed Al–Cu–Li alloys, the most significant precipitates are T_1 and $\theta'(Al_2Cu)$ [8]. T_1 forms platelet with a hexagonal structure on $\{111\}_{Al}$ planes [9]. Great efforts have been made to clarify the precipitation process and strengthening mechanism of T_1 in Al-Cu-Li alloys. Dislocations, octahedral voids, grain and sub-grain boundaries, GP_{T1} zones, Mg clusters forming on $\{111\}_{Al}$ planes and Al_3Zr particles have all been reported as providing heterogeneous nucleation sites for T_1 [10–12]. External stress applied during ageing induces a high density of elastic or plastic deformations, and the nucleation energy on these defects could be significantly lower than that of homogeneous nucleation [13]. The great increased number density of dislocation jogs provide more nucleation sites for the precipitation of T_1. The θ' phase is another strengthening phase in Al–Cu–Li alloys, such as 2090 and 2099, it, too, precipitates on $\{100\}_{Al}$ planes as platelets. Grain/subgrain boundaries, dislocations and Al_3Sc particles are considered to provide nucleation sites for θ' [14]. Stress loading during ageing could make the precipitation of T_1 and θ' into competition by competing Cu solutes. Zhu et al. observed stress induced fine denser preferential orientation of θ' in an Al–Cu alloy [15]. Ma et al. investigated the microstructural evolution of an Al–Cu–Li alloy with different stress levels [16]. They found that θ', $\sigma(Al_5Cu_6Mg_2)$ and T_1 played dominant roles in the low-level stress alloy, whereas T_1 became the major strengthening phase in the high-stress alloy. According to Cahn, the equilibrium T_1 phase has a lower volume free energy and is easier to nucleate on the dislocation jogs as compared with that of θ' [17]. Promoting the precipitation of T_1 could hinder the formation of θ' and σ by competing Cu solutes when higher levels of stress are applied. Jiang et al. also observed promoted precipitation of T_1 in a stress added Al-Cu-Li-Mg-Ag alloy [6]. So far, most of the effects of stress ageing on the precipitates of Al-Cu-Li alloys are mainly qualitative analysis, but lack of quantitative analysis.

The type, size, distribution and volume fraction of precipitates are important factors in the electrochemical and corrosion behaviour of the alloy. According to Li et al. the corrosion potential of T_1 in 0.6 M NaCl solution is approximately − 1076 mV/SCE, which is relatively more negative than that of the matrix [18]. When exposed to the electrolyte, T_1 forms a galvanic cell with the surrounding matrix, which preferentially dissolves as an anode. Heterogeneous precipitation always leads to

* Corresoponding authors.
E-mail address: xinhuajiangbo@163.com (B. Jiang).

https://doi.org/10.1016/j.corsci.2022.110314
Received 15 September 2021; Received in revised form 25 March 2022; Accepted 14 April 2022
Available online 22 April 2022
0010-938X/© 2022 Elsevier Ltd. All rights reserved.

preferential attack and local corrosion along the grain/subgrain boundaries and in non-uniformly precipitated grain interiors [19]. Promoted precipitation of T_1 in the grain interior could balance the potential difference between the grain/subgrain boundaries and grain interior, thereby causing the corrosion mode to evolve from intergranular corrosion (IGC) to intragranular corrosion in an Al–Cu–Li alloy [20]. In an aerated chloride solution, θ′ is usually noble with respect to the matrix. The corrosion potential has been reported as − 695 mV/SCE in 0.6 M NaCl solution, which is relatively more positive than that of the matrix [21]. After exposure of the alloy to the electrolyte, anodic dissolution of the matrix around the Al_2Cu precipitates leads to pitting, and the dissolution of the solute-depleted zone near grain boundaries enriched in Al_2Cu precipitates leads to intergranular corrosion.

However, precipitate alone is far from enough to clarify the corrosion behaviour of the alloy. According to Guerin et al., the precipitation of T_1 along the grain boundary is not necessary for the intergranular corrosion of an Al–Cu–Li alloy with T34 temper [22]. Corrosion occurs on the shared interface of two grains, one containing a low internal-misorientation ratio in one grain and the other a high one. A large difference in internal misorientation is the driving force for corrosion. They also analysed the effect of grain size on corrosion, but they found it less important than internal misorientation in explaining the corrosion behaviour of Al–Cu–Li alloy with T34 temper. Zhang et al. found that, in 2A97-T3 Al–Cu–Li alloy, un-recrystallised grains with a high fraction of low-angle grainboundaries (LAGBs) are more sensitive to corrosion than are those without LAGBs [19]. They concluded that grain stored energy (equals to high density of dislocations) plays decisive roles in the corrosion of sub-grain boundaries in the un-recrystallised grains. Those grain boundaries decorated by T_1 are more sensitive to corrosion than those decorated by the T_B phase. Polygonisation and recrystallisation can be observed heterogeneously with increasing strain during creep deformation. The process involves rearrangement of dislocations and the formation of low angle grainboundaries (LAGBs) and sub-structures.

Precipitation, polygonisation and recrystallisation occur simultaneously during creep ageing. Dislocations formed during deformation not only provide nucleation sites for precipitates but also favour the formation of substructures, such as LAGBs. Consequently, in the present case, the effects of stress ageing on the precipitation (Qualitative and quantitative analyzed by transmission electron microscope), grain structure and corrosion behaviour of an Al–Cu–Li alloy were systematically investigated.

2. Materials and methods

2.1. Materials

Al–Cu–Li alloy with a 20-cm thickness was provided by the Beijing Institute Aerial Materials. The metallurgical state of the as-received plate was T87. The chemical composition of the alloy was characterised by an inductively coupled plasma atomic emission spectrometer (ICP-AES, Spectro, Spectro Blue Sop); the results are shown in Table 1. A piece of plate with a thickness of 6 mm was cut from the as-received plate along the rolling direction (RD). This 6 mm plate was solutionised in a salt bath furnace at 530 °C for 3 h and then quenched in cold water. Then, the plate was cold rolled to a thickness of 2.7 mm. The cold rolled alloy sheet was machined along the rolling direction into the geometry shown in Fig. 1. The machined samples were solutionised in a salt bath furnace at 530 °C for 1 h, and then placed in a creep machine with an auxiliary heating furnace. Different stress levels (0, 100 and 150 MPa) were applied to the samples, which were then heated to 175 °C at a heating rate of 15 °C/min. Three thermocouples were placed around the sample to ensure temperature stability during creep ageing. After 31 h, the samples were quenched in cold water.

Table 1
Chemical composition of the as-received Al–Cu–Li alloy.

Element	Cu	Li	Mg	Mn	Zr	Al
Content/wt%	2.81	1.40	0.014	0.29	0.11	Bal.

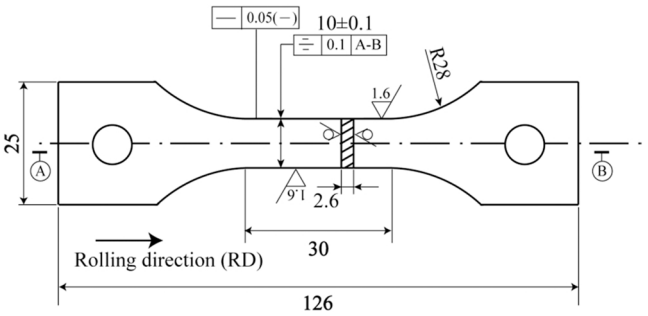

Fig. 1. Geometry of samples with different levels stress loading along the rolling direction.

2.2. Electrochemical and corrosion test

Creep ageing could have a significant impact on the precipitation, which plays a significant role in the electrochemical and corrosion behaviour of the alloy. Hence, a potentio-dynamic polarisation test was performed in the present case. The potentio-dynamic polarisation test was conducted in a conventional three electrode electrochemical cell composed by a Pt mesh electrode (auxiliary electrode), saturated calomel electrode (reference electrode) and working electrode (sample), with a scanning rate of 1 mV/SCE. The electrolyte was prepared by adding analytically pure NaCl reagent to deionized water to obtain a 0.6 M NaCl solution. Longitudinal–longitudinal–transverse (L-LT) surfaces with an area of 1 cm^2 exposed to the electrolyte were ground with a series of 400, 600, 800, 1000 and 1200 mesh grits followed by a 1 μm diamond paste polishing. The surfaces not exposed to the electrolyte were sealed by epoxy resin. Before testing, the samples were immersed in the electrolyte for 10 min to reach a stable voltage. The surface morphology of the samples after potentiodynamic polarisation test was observed using scanning electron microscopy (SEM; FEI Helios Nanolab 600i).

2.3. Qualitative and quantitative analysis of precipitates

Qualitative and quantitative analysis of precipitates has been carried by transmission electron microscope (TEM) and High-angle annular dark-field scanning transmission electron microscopy (HAADF-STEM). The samples were mechanical thinned to 80–100 μm by 400, 800 and 1000 grits, then punched into discs with a diameter of 3 mm. The discs were twin-jet electro-polished in a mixture of 25 vol% HNO_3 and 75 vol % methanol at a polishing temperature of − 25 ℃ and a voltage of 17 V. TEM observation was carried out by a FEI $G^2$20 with an operating voltage of 200 eV. HAADF-STEM observation was conducted by using a Titan $G^2$60–300 with an operating voltage of 300 eV. In qualitative analysis, selected area diffraction pattern and dark field images of the sample were obtained on the back focal plane by using parallel beam. Quantitative analysis of the precipitates was calculated by measuring the observed foil thickness using convergent beam electron diffraction (CBED).

2.4. EBSD analysis and quasi-in-situ observation

Electron back-scatter diffraction (EBSD) was used to analyse the grain structure of the alloy with and without stress addition. The samples were cut to have dimensions of 3 mm × 4 mm and then grounded using 400, 600, 800, 1000 and 1200 mesh grits. For aluminium alloys, the most widely used sample preparation method for EBSD analysis is

electrolytic polishing. However, an ion beam polishing system (Gatan 691) was used in the present case to avoid chemical etching of the surface, which would affect the subsequent quasi-in-situ corrosion observation. Ar^+ with an accelerating voltage of 4 kV and polishing angle of 2° was used to remove the stressed layer on the surface. Then, EBSD characterisation was carried out on the polished area using a FEI Helios Nanolab 600i with an accelerating voltage of 20 kV, and the data were analysed using the software of Channel 5. A quasi-in-situ observation was conducted by immersing the ion milled area in 0.6 M NaCl solution for 40 h, after which it was gently liberated and cleaned in absolute ethyl alcohol. The corroded surface was observed by SEM (FEI Helios Nanolab 600i).

3. Results and discussion

3.1. Electrochemical behaviour of alloy with different stress level

Fig. 2 shows the results of open-circuit potential (OCP) and potentio-dynamic polarisation measurements in 0.6 M NaCl solution carried out for alloys stress aged at 0, 100 and 150 MPa. The OCP of the 0 MPa stress-aged alloy was approximately − 0.671 V/SCE, and those of 100 and 150 MPa stress aged alloys were − 0.690 and − 0.703 V/SCE, respectively. Thus, OCP decreases with an increase in the stress level (Fig. 2a). In Fig. 2b, the shape of potential-dynamic polarisation curves is almost unaffected by different levels of stress ageing; the corrosion potentials of 0, 100 and 150 MPa stress-aged alloys as determined by Tafel-type extrapolation were − 0.667, − 0.682, and − 0.708 V/SCE, respectively. The evolutionary trend of the corrosion potential was thus consistent with that of the OCP. Grain size and sub-grain structure are reported to have less effect on the OCP and corrosion-potential evolution than precipitates in the alloy [21,23]. Proton et al. investigated the effect of ageing treatment on the electrochemical behaviour of 2055 Al–Cu–Li alloy and found that improved precipitation of T_1 in the grain interior causes the OCP and corrosion potential to move in a more negative direction [20]. In their investigation, the corrosion mode of intergranular corrosion (IGC) and intragranular corrosion by immersion in 0.7 M NaCl solution was consistent with that after polarisation test. In our previous investigation, we also found that the corrosion mode evolution of alloys immersed in the electrolyte for different ageing time duration was the same as that after polarisation test [24]. Hence, in the present case, the effect of different levels of stress on the alloy corrosion mode evolution was only observed after the polarisation test.

3.2. Corrosion mode evolution with different stress level

Fig. 3 shows the SEM images of 0, 100 and 150 MPa stress aged alloy L-LT surfaces after the polarisation test in 0.6 M NaCl electrolyte. Preferential corrosion defects in Fig. 3a can be observed in parts of the surface area. Preferential dissolution of grain boundaries (as shown in Fig. 3b) causes entire grains to fall off from the alloy (local IGC). Few corrosion bands can be observed in the grain interior, as shown in Fig. 3c. After loading the alloy at 100 MPa during ageing at 175 °C, the corrosion mode of the alloy was mainly local intragranular corrosion, as shown in Fig. 3d and e. The density of corrosion bands in the grain interior (Fig. 3f) was remarkably increased compared with that of the 0 MPa stress aged alloy. With a further increase in stress loading (to 150 MPa) , the corrosion behaviour of the alloy was mainly local intragranular corrosion, and the corrosion bands disappeared completely. To improve the reliability of the previous corrosion mode evolution with stress loading, the alloy was cut along the longitudinal-short transverse (L-ST) plane, and the corrosion mode was observed by using an optical metallographic microscope after grinding and polishing. The results are shown in Fig. 4. Here, the corrosion mode evolved from local IGC to local intragranular corrosion with stress loading, which is consistent with the observation of the L-LT surface.

3.3. Quantitative and qualitative analysis of precipitates before corrosion

The electrochemical behaviour and corrosion mode evolution as reported above are closely related to the precipitates in the grain interior and along the grain boundary. Hence, qualitative and quantitative analyses were carried out here to establish the relationship between the corrosion behaviour and precipitates in the alloy. Qualitative analysis was conducted by selective electron diffraction pattern and dark field images of TEM. As shown in Fig. 5b, f and j, diffraction spots of 1/2 $\{220\}_{Al}$ and 1/2 $\{220\}_{Al}$ and streaks across the $\{020\}_{Al}$ and $\{002\}_{Al}$ were observed along $[001]_{Al}$ zone axes of all the variously stress aged alloys. In Al–Cu–Li alloy, δ′ precipitates from the matrix as spherical morphology with a cube-cube orientation, and its crystal structure is reported to be cubic with lattice parameter a= 0.401 nm. By contrast, θ′ forms a tetragonal structure with rectangular or octagonal plate morphology, and its orientation relationship with the matrix is $(100)_{Al}//(100)_{\theta'}$ and $[001]_{Al}//[001]_{\theta'}$. Hence, the diffraction spots of $1/2\{220\}_{Al}$ and $1/2\{200\}_{Al}$ were attributed to the δ′ phase, while streaks along $\{020\}_{Al}$ and $\{002\}_{Al}$ originated from the θ′ phase. An aperture was placed on DF1 in Fig. 5b, f and j, the corresponding dark field images are shown in Fig. 5a, e and i. It can be observed that θ′ phase is the main strengthening phase along $[001]_{Al}$ zone axes in these alloys, and its size decreases remarkably with increase levels of tensile stress. Moreover, θ′ precipitates preferentially along a certain cube plane of the matrix in the 150 MPa stress aged alloy (Fig. 5i). In Al-Cu alloys, William et al. also found that when the tensile stress loading direction was parallel to one of the $[100]_{Al}$ directions, the precipitation of the variant on $(100)_{Al}$ cube plane was parallel to the loading direction would be favoured, the other two variants on $(010)_{Al}$ and $(001)_{Al}$ should be inhibited [25]. He suggested that the tensile stress could relax the strain between the matrix and precipitate and favour nucleation on that plane.

Looking along the $[112]_{Al}$ zone axes, intense diffraction spots and

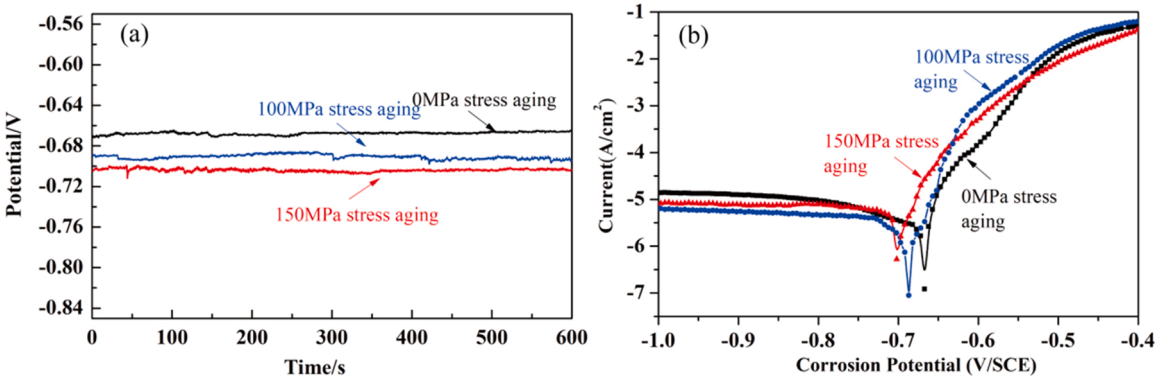

Fig. 2. Open-circuit potential (a) and potentio-dynamic polarisation curves (b) plotted in 0.6 M NaCl solution for alloys with different levels stress ageing.

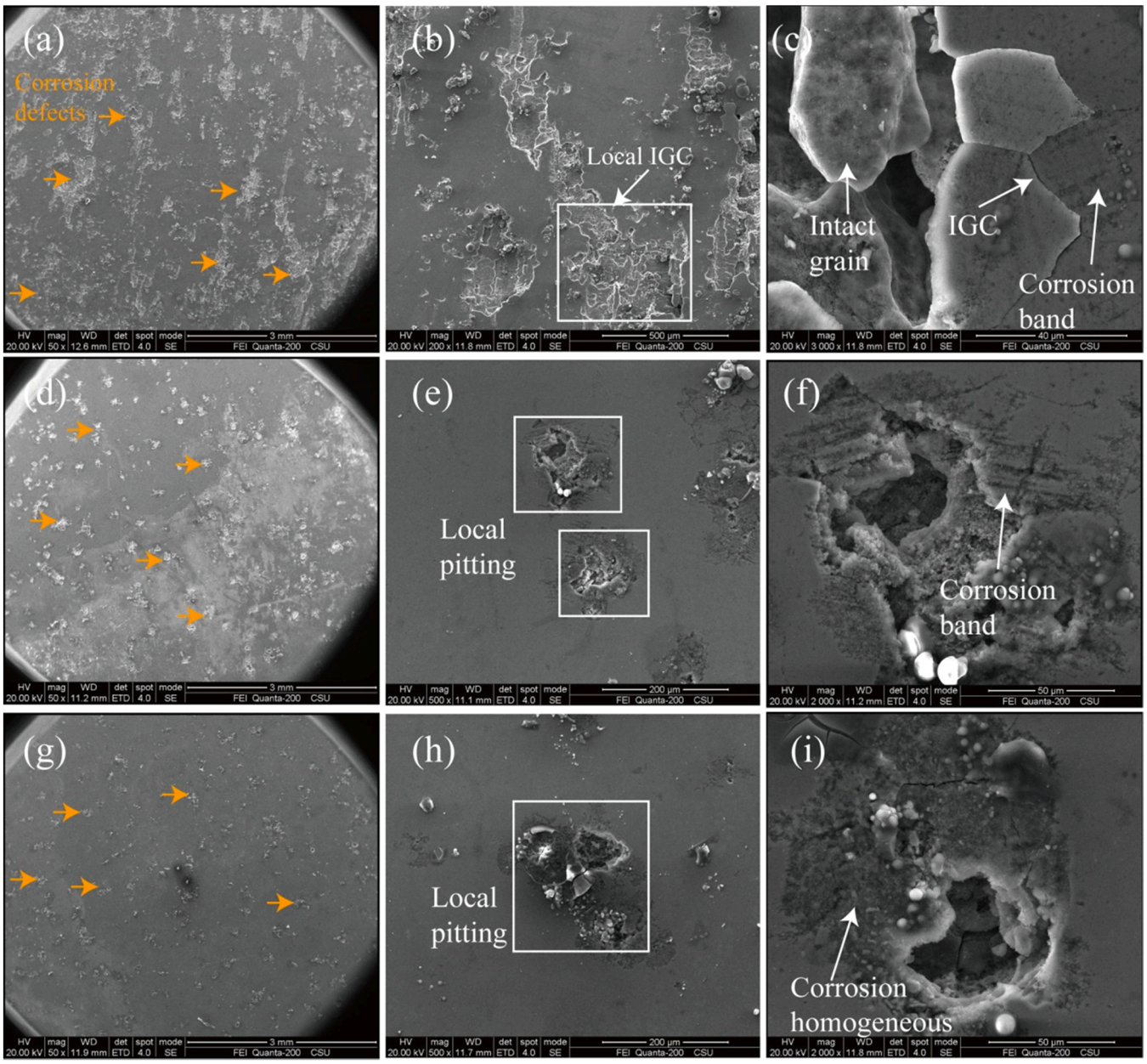

Fig. 3. SEM images of the corrosion morphology of L-LT surface of the Al–Cu–Li alloy without stress ageing (a, b, c) and with 100 MPa stress ageing (d, e, f) and 150 MPa stress ageing (g, h, i) at 175 °C after polarisation test in 0.6 M NaCl solution.

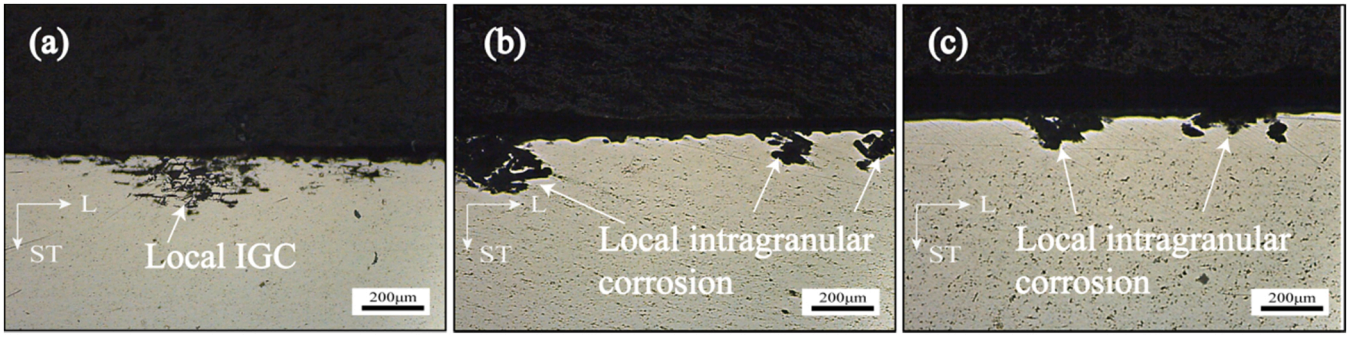

Fig. 4. Cross section of the L-ST plane of 0 MPa (a), 100 MPa (b) and 150 MPa (c) stress aged alloy after polarisation test in 0.6 M NaCl solution.

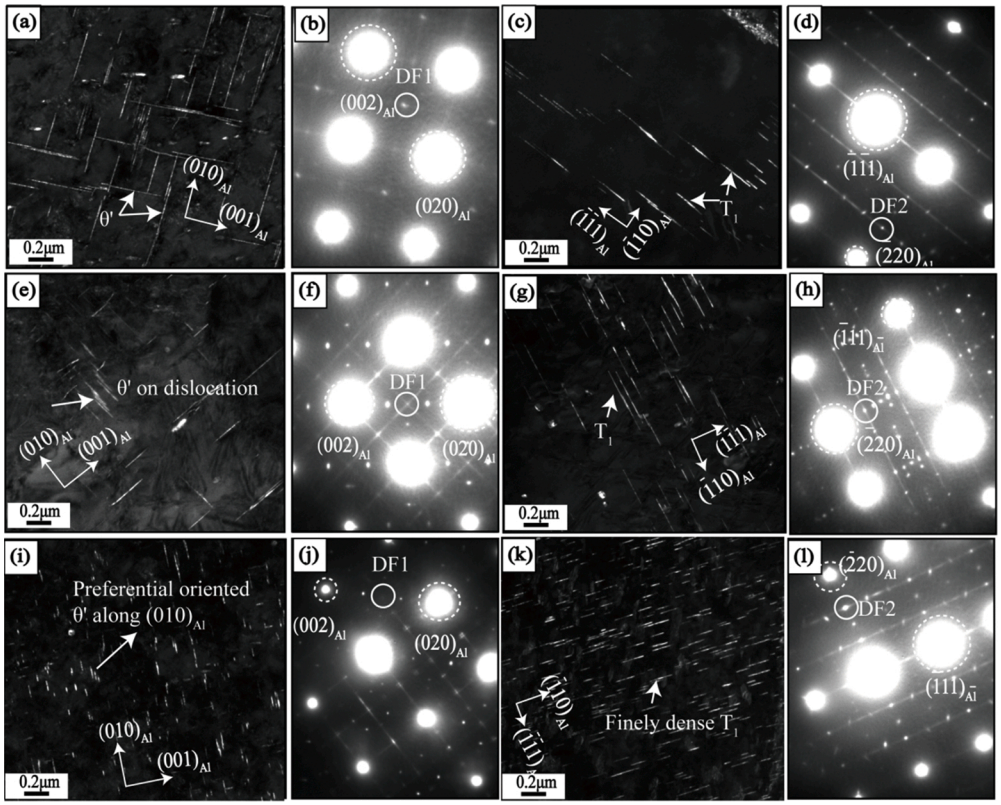

Fig. 5. Dark field images (a, c, e, g, i, k) and selected electron area diffraction patterns (b, d, f, h, j, l) of Al-Cu-Li alloy without (a, b, c, d) and with 100 MPa (e, f, g,h), 150 MPa (I, j, k, l) near $[100]_{Al}$ (a, b, e, f, i, j) and $[112]_{Al}$ (c, d, g, h, k, l) zone axes.

streaks of T_1 can be observed at $1/3\{2\bar{2}0\}_{Al}$ (Fig. 5d, h, l). An aperture has been placed on DF2 in Fig. 5d, h, l, and the dark field images obtained are shown in Fig. 5c, g and k. The size of T_1 was greatly refined as loading stress increased during ageing. T_1 is an equilibrium plate phase that partially coherent with the matrix, its crystal structure is hexagonal. The thin plate-like hexagonal phase on $\{111\}_{Al}$ planes was mainly

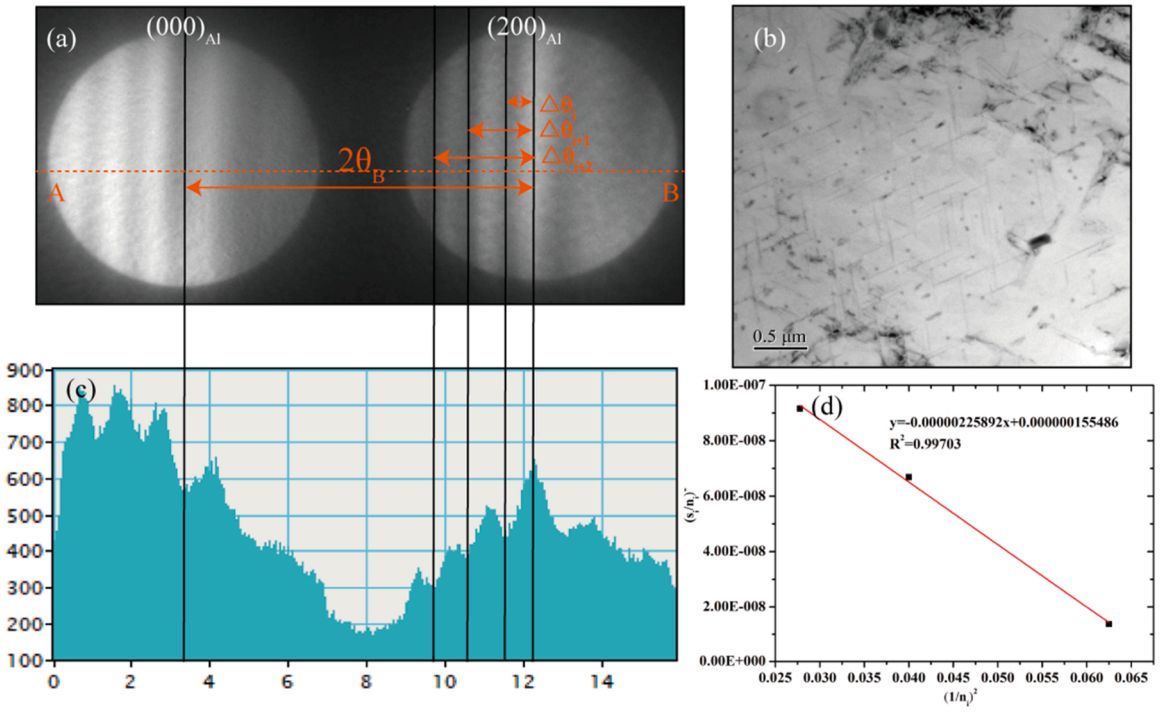

Fig. 6. Key parameters for precipitates quantitative analysis in the 0 MPa stress aged alloy: CBED pattern (a), platelet precipitates of the observed area along $[110]_{Al}$ (b), the intensity line profile from A-B (c) and the relationship between $\left(\frac{s_i}{n_i}\right)^2$ and $\left(\frac{1}{n_i}\right)^2$ (d).

formed by the decomposition of b = 1/2 < 110 > perfect dislocations into b = 1/6 < 112 > partial dislocations. Stress loading significantly increased the density of dislocations in the matrix, and thus the number of nucleation sites for T_1, making the precipitate more finely dispersed. In summary, stress ageing has little effect on the types of precipitates in the present case but does cause size refinement and preferred precipitation.

To understand the corrosion performance in more detail, quantitative analysis was carried out in 0 and 150 MPa stress-aged alloys. The thickness of the observed area should be measured for a quantitative analysis. Although there are many ways to measure thickness (e.g. CBED, electron energy loss spectroscopy (EELS) and so on), CBED was adopted in the present case owing to its high accuracy [26,27].

In a two beam condition, a bright disc of $(000)_{Al}$ and a dark disc of $(200)_{Al}$ can be observed from the CBED pattern, as shown in Fig. 6a and Fig. 8a. The foil thickness of the observed area can be calculated by the deviation of *i*-th from the exact Bragg position (s_i) and the extinction distance ε_g of the alloy. s_i can be obtained by the following equations [28]:

$$\left(\frac{s_i}{n_i}\right)^2 = -\frac{1}{\varepsilon_g^2}\bullet\frac{1}{n_i^2}+\frac{1}{t^2} \tag{1}$$

Where

$$s_i = \frac{\lambda}{d_{hkl}^2}\bullet\frac{\Delta\theta_i}{2\theta_B} \tag{2}$$

λrepresents the wavelength of the electron beam, $\Delta\theta_i$ indicates the distance from each black line to the centre of the bright Kikuchi line in $(200)_{Al}$ diffraction disc. θ_B represents the Bragg angle of $(200)_{Al}$, and d_{hkl} is the spacing of the operating reflection. From Eq. (2), the value of s_i can be calculated by measuring $\Delta\theta_i$and $\theta_B$in Fig. 6a and Fig. 8a. Eq. (1) is a linear equation in $(1/n_i)^2$, the foil thickness can be calculated by plotting $(s_i/n_i)^2$ and finding the intercept of the line. Hence, gradually increase the trial calculation of n_1, n_2,n_3…(n_1=1, n_2=2, n_3=3 and so on) until all the values of $(s_i/n_i)^2$fall on a straight line, as shown in Fig. 6d and Fig. 8d. The resulting calculated thicknesses were 253.6 nm for 0 MPa stress aged alloy and 166.8 nm for 150 MPa stress aged alloy.

For 0 MPa stress aged alloy, the number density and volume fraction of the precipitates were calculated based on two simplifications: (1) the precipitates in each grain are the same; (2) the number of variants on each habit plane is the same. To prevent the contrast in the bright field image from affecting the size statistics of the precipitates, dark field images were adopted. The size was measured using the software of Image J. More than five images were used to ensure statistical significance. The average size of T_1 was 328.3 nm and that of θ′ was 238.1 nm. The number of T_1 in the observed area for thickness measurement in Fig. 6b is 75 and that of θ′ was 17. The thickness of T_1 observed from the HAADF-STEM images in Fig. 7a was two layers. One layer of T_1 precipitates is approximately equal to five $\{111\}_{Al}$ plane spacing, or about 1.15 nm, adding a layer of T_1 was equivalent to increasing the spacing of the four $\{111\}_{Al}$ plane by approximately 2.07 nm [29].

The volume fraction (v_f) of T_1 and θ' was calculated using the equations:

$$v_f^{T_1} = \frac{2\times V_{[110]}^{T_1}}{V_{observe}} \tag{3}$$

$$v_f^{\theta'} = \frac{3\times V_{[110]}^{\theta'}}{V_{observe}} \tag{4}$$

where $V_{[110]}^{T_1}$ and $V_{[110]}^{\theta'}$ are the volumes of T_1 and θ' viewed along $[110]_{Al}$ zone axes, respectively.

$$V_{[110]}^{T_1/\theta'} = \frac{1}{4}\pi N_{T_1/\theta'}^{[110]}\times\left(D_{T_1/\theta'}\right)^2\times t_{T_1/\theta'} \tag{5}$$

Here, $N_{T_1/\theta'}^{[110]}$ represents the number of T_1/θ' in Fig. 6b. $D_{T_1/\theta'}$ is the diameter of T_1/θ' and $t_{T_1/\theta'}$ is its thickness. $V_{observe}$is the volume of the observed region of the foil.

$$V_{observe} = A_{observe}\times T_{observe} \tag{6}$$

Here, $A_{observe}$ represents the area of the observed foil, and $T_{observe}$ represents the corresponding foil thickness. The volume fractions of T_1 and θ' in the 0 MPa stress aged alloy calculated from Eqs. (3–6) were 1.06% and 0.24%, respectively.

The number density can be obtained as follows [30]:

$$n_{T_1/\theta'} = \frac{n'_{T_1/\theta'}}{V_{observe}} \tag{7}$$

where $n'_{T_1} = 2\times N_{T_1}^{[110]}$ and $n'_{\theta'} = 3\times N_{\theta'}^{[110]}$. The number densities of T_1 and θ' calculated from Eq. 7 were 0.43×10^{20}/mm^3 and 0.15×10^{20}/mm^3, respectively.

Fig. 5 shows that θ′ precipitates preferentially when the stress level increased to 150 MPa. Therefore, the volume fraction and number density cannot be calculated using Eq. (4) for stress free alloy. Zhu et al. conducted a statistical analysis on the number of θ′ parallel and

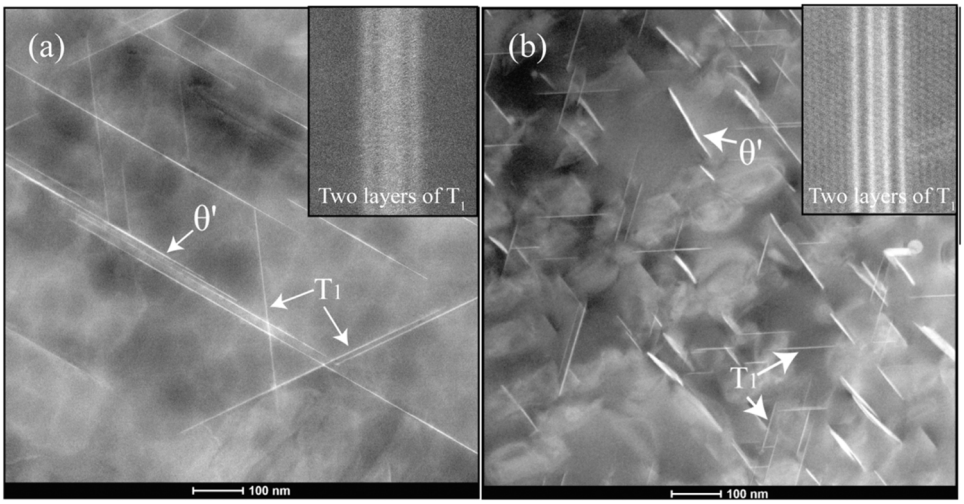

Fig. 7. HAADF-STEM images of 0 MPa stress aged alloy (a) and 150 MPa stress aged alloy (b) viewed along $[110]_{Al}$ zone axes.

perpendicular to the loading direction in stress aged Al–Cu alloy, and found that the number ratio of θ′ perpendicular to the loading direction was 0–9% [15]. Therefore, 4.5% was adopted in the present case for the quantitative analysis of θ′ making Eq. (4):

$$v_f^{\theta'} = \frac{V_{[110]}^{\theta'} \times (2 + 4.5\%)}{V_{observe}} \tag{8}$$

The volume fraction of θ′ in the 150 MPa stress aged alloy was 0.69%, and the number density calculated from Eq. (8) was $0.96 \times 10^{21}/\mathrm{mm}^3$. The $n'_{\theta'}$ in Eq. (7) was taken to be $n'_{\theta'} = N_{\theta'}^{[110]}(2 + 4.5\%)$.

It is well known that T_1 precipitates from the matrix along $\{111\}_{Al}$ plane. Four variants of T_1 inclined approximately 54.7° to the $[001]_{Al}$ zone axes, and the intensities of their diffraction spots at $1/4(024)_{Al}$, $1/4(042)_{Al}$, $1/3(022)_{Al}$ and $2/3(022)_{Al}$ were approximately identical. Therefore, the number density and volume fraction of T_1 on each habit plane of $(111)_{Al}$ can be assumed to be the same in stress aged and stress free alloys. The average length of T_1 measured from five TEM dark field images was 89 nm, and the number of T_1 in the observed area for foil thickness measurement was 174 (Fig. 8b). Based on the investigation of Dorin, the activation thickening of T_1 is mainly controlled by the ageing temperature, and stress has little influence [29]. The HAADF-STEM images in Fig. 7b reveal that the number of T_1 layers in the stress aged alloy was equal to that in the stress free alloy; the thickness was approximately 2.07 nm.

The volume fraction and number density calculated from Eqs. 3, 5 and 7 were 3.54% and $3.02 \times 10^{21}/\mathrm{mm}^3$, respectively.

According to the results of the qualitative and quantitative analyses, T_1 is the most predominant precipitate for strengthening in both stress-free and stress-added alloys. Stress loading results in an approximately doubled volume fraction of T_1 in the grain interior. As summarised in the introduction, the corrosion potential of T_1 was − 1076 mV/SCE, and improved T_1 precipitation induced the corrosion potential of the alloy move to the more negative direction. Moreover, promoted precipitation of T_1 consumes a large amount of Cu solutes from the matrix, and the corrosion potential should be further lowered. Therefore, the OCP and corrosion potential of the 150 MPa stress-aged alloy were remarkably more negative than those of 0 MPa stress-aged alloy, as shown in Fig. 1. The potential difference caused by precipitates in the intragranular and on grain boundaries is the main factor for corrosion mode evolution. Fig. 9 shows dark field and bright field images of the grain and sub grain-boundaries of 0 MPa and 150 MPa stress aged alloy along the $[001]_{Al}$ and $[112]_{Al}$ zone axes. In the unstressed aged alloy, a small amount of θ′ could be observed (Fig. 9a), and T_1 segmented continuously on the sub grain boundary and grain boundary (Fig. 9b and Fig. 9c). Moreover, there was far less precipitation in the grain interior than along the grain and sub grain boundaries. Corrosion potential on the grain boundary could be more negative than that in the grain interior. The grain boundary dissolves as an anode, leading to IGC. The corrosion medium could penetrate to the subsurface along the grain boundary owing to the continuous precipitation of T_1. Simultaneously, corrosion also occurs on the slip bands with preferential precipitation of coarse T_1, appearing as corrosion bands in the grain interior. Here, the corrosion mode is mainly IGC with minimal intragranular corrosion, as shown in Figs. 3 and 4. In the 150 MPa stress-aged alloy, numerous dislocations could be produced to provide nucleation sites for T_1. Previous quantitative analyses show that the volume fraction of T_1 increase from 1.06% to 3.54%. Promoted intragranular precipitation consumes a large amount of Cu solute in the matrix, and suppresses the precipitation of T_1 along the subgrain/grain boundary. Hence, segregation of T_1 is rarely observed on the sub grain and grain boundaries, as shown in Fig. 9e and f. The promoted intragranular precipitation and suppressed grain boundary precipitation of T_1 shortened the potential difference between the intragraunlar and subgrain/grain boundaries. It is also possible that the intragranular potential was slightly lower than the grain boundary. Hence, the corrosion mode evolved into intragranular corrosion. Dissolution of the fine, dense uniform distribution of active T_1 results in micro pits and uniform corrosion in the grain interior; this observation was different from that in 100 MPa stress-aged alloy. The severe corrosion bands in

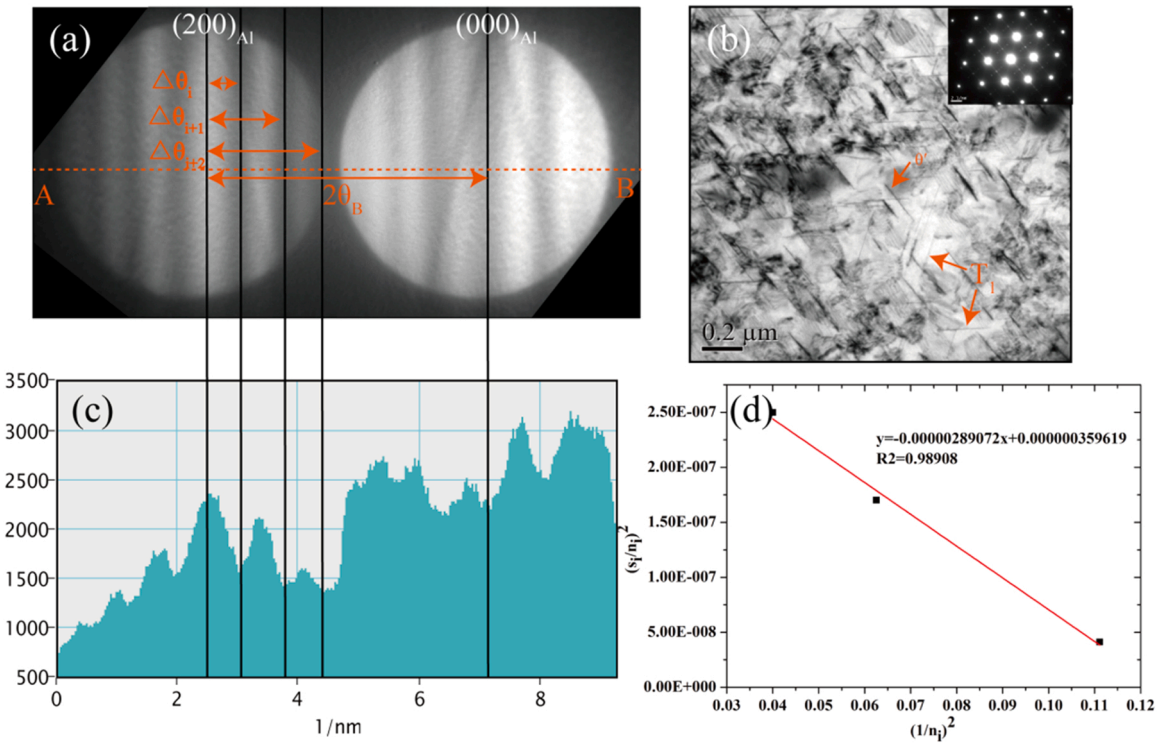

Fig. 8. Key parameters for precipitates quantitative analysis in the 150 MPa stress aged alloy: CBED pattern (a), platelet precipitates of the observed area along $[110]_{Al}$ (b), the intensity line profile from A-B (c) and the relationship between $\left(\frac{S_i}{n_i}\right)^2$ and $\left(\frac{1}{n_i}\right)^2$ (d).

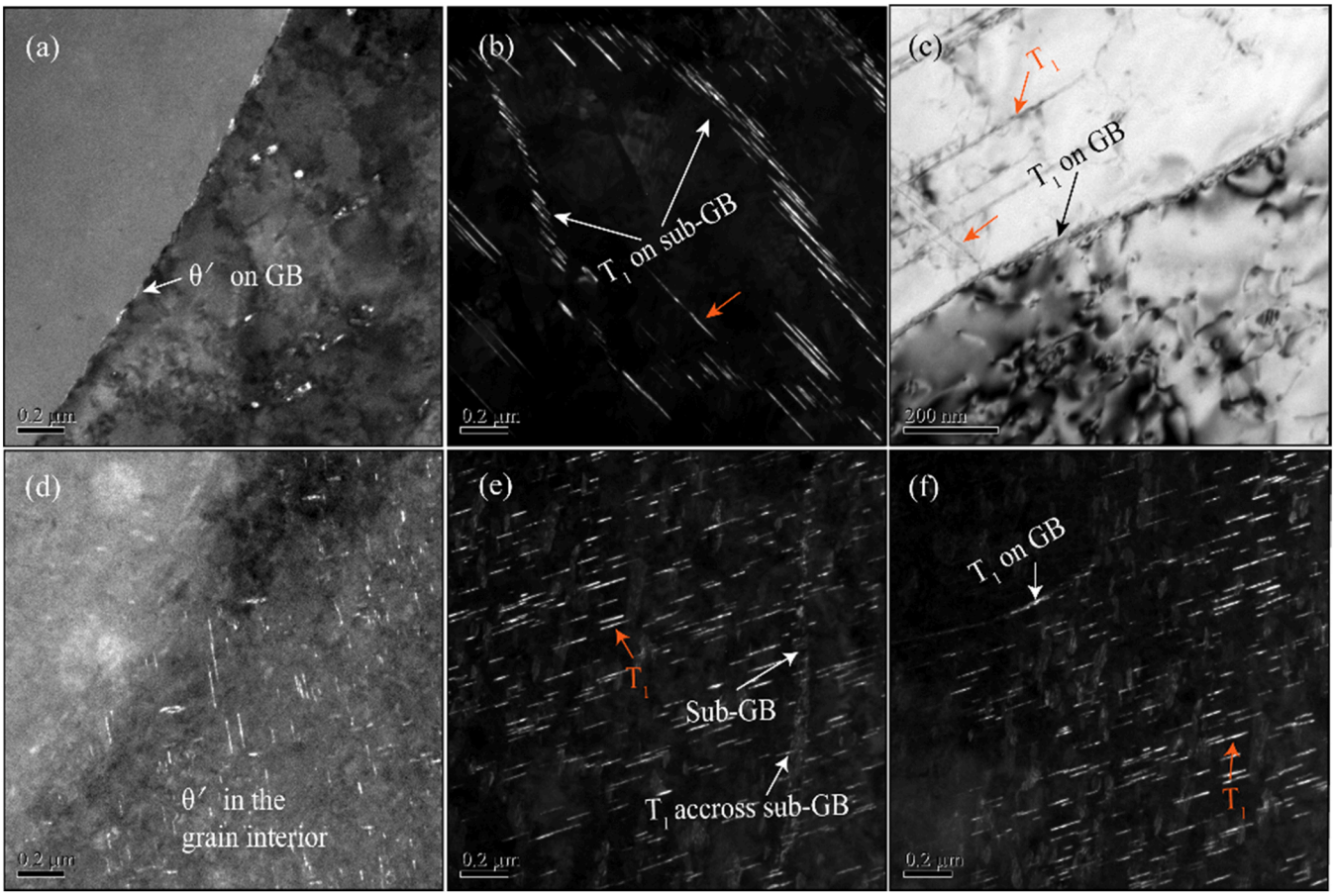

Fig. 9. Dark field image (a-b), (d-f) and bright field image (c) of 0 MPa (a-c) and 150 MPa (d-f) stress aged alloy grainboundary view along $[100]_{Al}$ zone axes (a),(d) and $[112]_{Al}$ zone axes (b-c), (e-f).

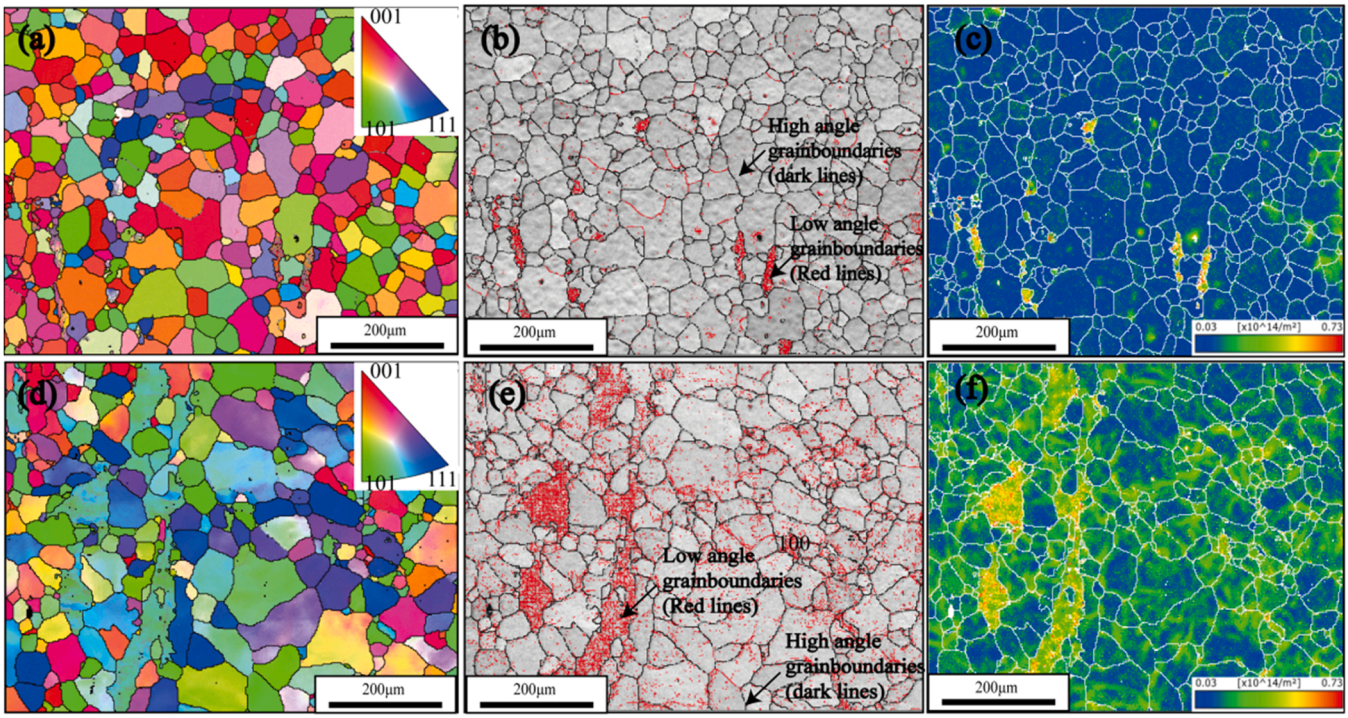

Fig. 10. EBSD (IPF-Z0) micrograph (a, d), grain boundary (b, e),dislocation density(c, f) of 0 MPa (a-c) and 150 MPa (d-f) stress aged Al-Cu-Li alloy before immersing in 0.6 M NaCl solution for 42hrs.

the grain interior of the 100 MPa stress-aged alloy were caused by promoted precipitation of T_1 with a size equal to that of 0 MPa stress-aged alloy (Fig. 5), as shown in Fig. 3f and i. The precipitation of T_1 modified by 150 MPa stress loading could substantially slow down the penetration rate of electrolyte to the subsurface and consequently reduce the severity of intragranular corrosion, as shown in Fig. 3g to Fig. 3i and Fig. 4c.

3.4. Grain structure

However, the IGC of the 0 MPa stress aged alloy and intragranular corrosion of the 150 MPa stress aged alloy are localised, as shown in Fig. 3. Preferential attack on grain boundary and grains could be observed. Precipitates and their distributions are insufficient to explain the localised corrosion behaviour of these alloys. Grain structures such as dislocation density, low and high angle grain boundaries, grain orientation and misorientation have been reported to be responsible for the localised corrosion in alloys. Here, the alloy suffered cold rolling, solid solution and artificial ageing, and nearly all the deformed grains were recrystallised during the solid solution, as shown in Fig. 10a. A higher fraction and density of low angle grain boundaries (red lines in Fig. 10b) and dislocations (in Fig. 10c, gradual change in colour from blue to red indicates a gradual increase in dislocation density) could be observed in the unrecrystallised grains in the 0 MPa tress aged alloy. In the 150 MPa stress aged alloy, most of the grains were recrystallised, as shown in Fig. 10d. A high fraction of LAGBs and high density dislocations were observed in both recrystallised and unrecrystallised grains (Fig. 10e and f). It is known that grains stored a large amount of energy in the form of dislocations during deformation. The energy is released in recovery, recrystallisation and grain coarsening. M.E.Kassner proposed that dynamic recovery and recrystallisation occur during the creep process [31]. The recovery process lowered the stored energy by dislocation rearrangement and formed LAGBs. With continuous stress loading, LAGBs absorb new dislocations produced in the matrix and form high angle grain boundaries (HAGB) and new recrystallised grains. Thus, a considerable increase in LAGBs and dislocation density could be observed in stress loaded alloys. Quantitative analysis of LAGBs and geometrically necessary dislocations (GND) in 0 and 150 MPa stress aged alloy shows that the length fraction of LAGBs in the 150 MPa stress aged alloy (62.2%) is approximately three times that of 0 MPa stress aged alloy (24.6%), and the density of GNDs is almost doubled by stress loading, as shown in Table 2.

Zhang et al. reported that localised IGC mainly occurs along sub grain boundaries in unrecrystallised grains, and they also found that sub grains with higher stored energy exhibit higher IGC susceptibility [32, 33]. A shared interface with a significantly different fraction of LAGBs in the grains on both sides should be sensitive to IGC. Furthermore, grains with a higher density of dislocations (implying higher stored energy) are preferentially corroded. The increased ratio of LAGBs and dislocations caused by stress loading seems to enhance the susceptibility of the alloy to corrosion. However, the number of corrosion defects in the 150 MPa stress aged alloy greatly was much less than that in the 0 MPa stress aged alloy, and equal to that in the 100 MPa one, as shown in Fig. 3a, Fig. 3d and Fig. 3g. Quasi-in-situ EBSD corrosion observation was then carried out to clarify the dominant metallurgical parameters characterising the localised corrosion behaviour of the stress free and stress aged alloys.

Table 2
Fraction of low angle grain boundary, high angle grain boundary and GND density in 0 MPa and 150 MPa stress aged Al–Cu–Li alloy.

Stress level	Low angle grain boundary fraction (%) (1–15°)	High angle grain boundary fraction (%) (≥15°)	GND (1×10^{14}/ m^2)
0 MPa	24.6	75.4	19
150 MPa	62.2	37.8	31.2

3.5. Quasi-in-situ EBSD corrosion observation

Fig. 11a–d show the inverse pole figure (IPF) images, grain boundaries and dislocations of the observed area before immersion in 0.6 M NaCl electrolyte for 40 h and SEM images of the observed area in the stress free L-LT surface after immersion. The corroded areas were divided into four zones (1, 2, 3 and 4), and the grains with grain boundary corrosion were designated as G1-G9. The parameters of the corroded grains (adjacent grain size, GND and misorientation) are listed in Table 3. It can be seen that nearly all the corroded grain boundaries were HAGBs, and these grains are coloured in blue in Fig. 11a, which indicates that they were more closely oriented to $(111)_{Al}$. Among all the grains, the grain boundaries of G1, G3, G5, G6, G8 and G9 were all corroded, while G2 and G7 showed corrosion in some of the grain boundaries. The corroded and uncorroded grain boundaries were randomly distributed, it seems that the localised corrosion had nothing to do with the nearby grain GND density, misorientation or grain size of the alloy. Moreover, the shared interface with different densities of LAGBs and dislocations of grains on either side (Fig. 11b and c, zone 3) remained intact, as shown in Fig. 11g. In summary, grain orientation and HAGB are the most relevant for localised corrosion in the 0 MPa stress aged alloy.

Fig. 12 shows the IPF images, LAGB and GND of the observed area of the 150 MPa stress aged alloy before immersion and the SEM image of the same area after immersion in 0.6 M NaCl solution. The corroded defects in Fig. 12a were divided into four zones (1, 2, 3 and 4), and the corroded grains in these zones were designated as G1, G2, G3, G4–1, G4–2 and G5. It can be seen that the corroded grains are mainly oriented to $(111)_{Al}$. Stress loading during ageing leads to different degrees of deformation inside the grain. As seen in Fig. 12c, the GND densities in different regions within the same grain are different. In Fig. 12e, Fig. 12f and Fig. 12g, regions with high dislocation densities in G1, G2 and G4–2 showed no corrosion or very slight corrosion. The corroded grains oriented along the $(111)_{Al}$ did not show a correlation with the dislocation distribution. Furthermore, the grains in zone 4 with a high fraction of LAGBs and dislocations were intact after immersion, as shown in Fig. 12h. The enhanced fraction of LAGBs and dislocations caused by stress adding has no effect on the corrosion susceptibility of the alloy, and similar to the findings in the 0 MPa stress aged alloy, grain orientation was the main metallurgical parameter for local corrosion. More results of quasi-in-situ EBSD corrosion observation was attached in the supplementary materials.

As seen from the above experimental results, localised corrosion mainly occurs in the grains oriented to $(111)_{Al}$ in both 0 and 150 MPa stress-aged alloy. For grains with different crystallised orientations ($(111)_{Al}$, $(110)_{Al}$, $(100)_{Al}$), their corrosion behaviour was elucidated by preparing pure recrystallised single aluminium. Previous studies have reported that grains oriented close to $(001)_{Al}$ planes display the lowest dissolution rate, while those oriented to $(111)_{Al}$ planes exhibit the highest rate [34–36]. They considered that the $(111)_{Al}$ planes were the densest planes in pure aluminium, and its corrosion potential was more negative than those of grains with other orientations. Therefore, the driving force of corrosion in grains oriented to $(111)_{Al}$ planes could be larger than that for grains oriented to other orientations, thereby leading to localised corrosion. In Al–Cu–Li alloys with T3 temper, grains with a high density of LAGBs and dislocations are reported to be sensitive to corrosion, and in alloys with T8 temper, grains oriented to $(111)_{Al}$ are the most relevant to corrosion. Both T3 and T8 alloys are pre-deformed before ageing, and the deformation induces high density of dislocations, which are significant nucleation sites for T_1. However, the precipitation kinetics of alloys that undergo natural ageing (T3) is remarkably slower than those of alloys with artificial ageing (T8). Hence, a minimal amount of GP_{T1} is seen in alloys with T3 temper, and numerous dislocations remain. The impact of corrosion caused by T_1 is negligible. Grains with high fraction of dislocations and LAGBs indicate high stored energy. Therefore, the driving force for the corrosion of these grains are possibly

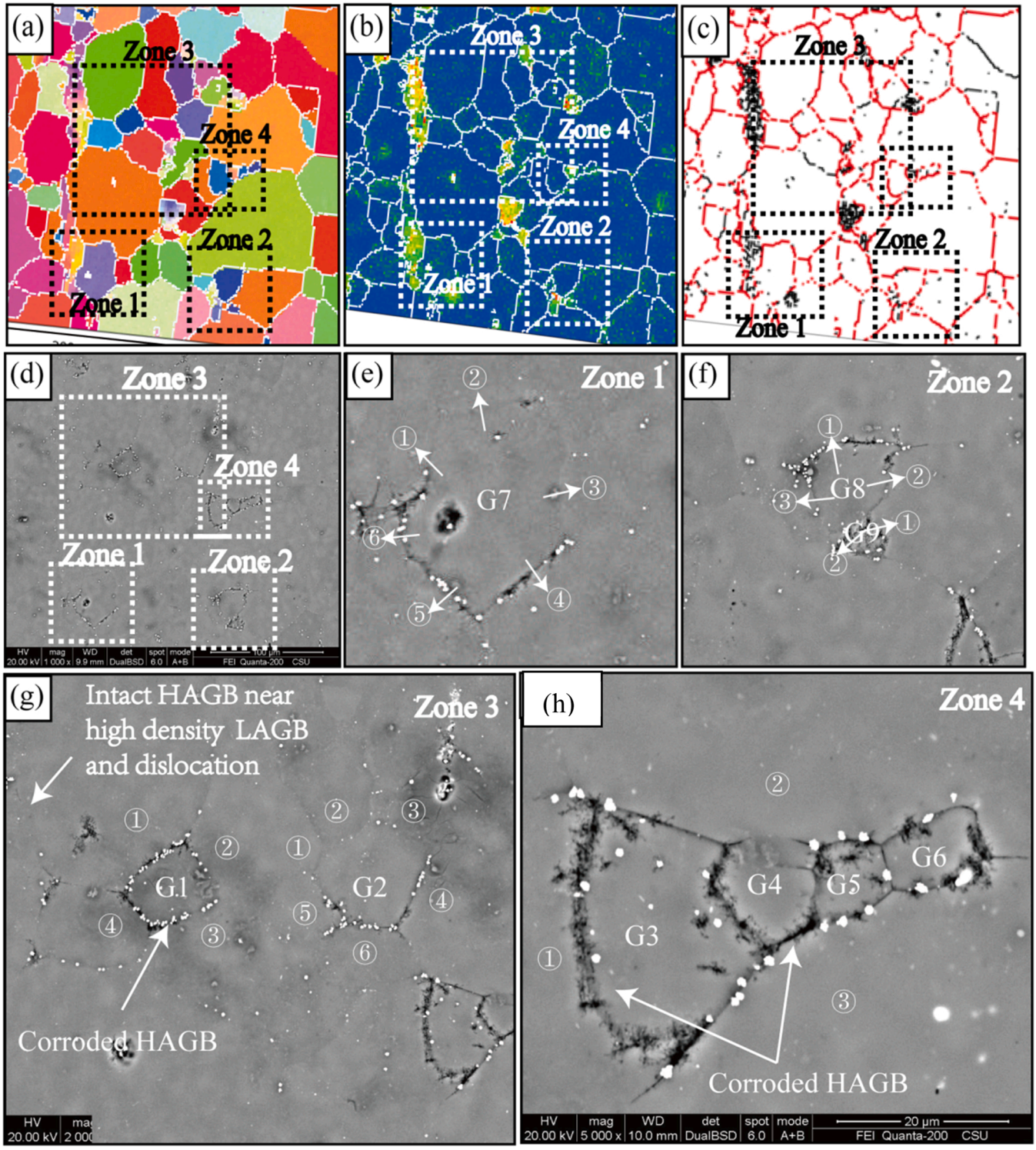

Fig. 11. Quasi-in-situ observation of the stress free alloy L-LT surface after immersing in 0.6 M NaCl electrolyte for 40hrs: EBSD (IPF-Z0) micrograph (a), grain-boundaries (b) and GND (c) of 150 MPa stress aged alloy before immersing; (d-h) were SEM micrographs of corroded defects of the EBSD observed area after immersing.

larger than that of grains oriented to $(111)_{Al}$. In Al–Cu–Li alloys with T8 temper, precipitation of T_1 is promoted, and most of dislocations disappear as the nucleating sites for T_1. Notably, $(111)_{Al}$ is the habit plane of T_1 phase, and the orientation relationship between the matrix and T_1 is $(0001)_{T1}//(111)_{Al}$. The basal planes of T_1 investigated by Donnadieu et al. [37] using HAADF and small-angle X-ray scattering could be Al–Li mixed layers, which could induce a more negative and active $(111)_{Al}$ plane in Al–Cu–Li alloys. The driving force of $(111)_{Al}$ planes for corrosion is expected to be much larger than that of grains with high density of dislocations and LAGBs due to the precipitation of T_1. Hence, among dislocation density, LAGBs, grain size and grain orientation, which factor is decisive for localised corrosion of the alloy mainly depends on the corrosion driving force. In the 0 MPa and 150 MPa stress-aged alloys in this study, the quantitative and qualitative

Table 3
Grain size, GND and misorientation of grains besides the interfaces of the corroded grains.

Corroded grain	Adjacent grain	Misorientation/ °	Adjacent grain size/ μm	Grain size difference	Adjacent grain GND/ $1 * 10^{14}/m^2$	Grainboundary between G1/~G8 and adjacent grain
G1	G1	–	22.34	–	0.2	–
	①	41.92	64.7	42.36	0.16	C
	②	60.39	52.2	29.86	0.14	C
	③	52.64	34.37	12.03	0.16	C
	④	19.91	27.27	4.93	0.19	C
G2	G2	–	29.85	–	0.18	–
	①	32.48	52.2	22.35	0.14	UC
	②	14.44	30.61	0.76	0.16	UC
	③	49.69	28.72	1.13	0.44	UC
	④	56.93	73.96	44.11	0.15	C
	⑤	32.19	30.02	0.17	0.19	C
	⑥	44.15	22.68	7.17	0.23	PC
G3	G3	–	22.79	–	0.16	–
	G4	43.47	10.59	12.20	0.22	C
	①	60.01	25.23	2.44	0.12	C
	②	47.05	73.96	51.17	0.14	C
	③	51.03	92.5	69.71	0.16	C
G4	G4	–	10.59	–	0.22	–
	G5-G6	42.98	13.54	2.95	0.24	C
	②	33.67	73.96	63.37	0.14	C
	③	31.29	92.5	81.91	0.15	PC
G5 +G6	G5 +G6	–	13.54	–	0.24	C
	②	53.38	73.96	60.42	0.14	C
	③	42.38	92.5	78.96	0.15	PC
G7	G7	–	39.09	–	0.2	–
	①	25.42	35.25	3.84	0.37	PC
	②	55.87	97.33	58.24	0.16	UC
	③	39.91	17.91	21.18	0.18	UC
	④	58.30	58.06	18.97	0.21	C
	⑤	21.43	24.10	14.99	0.18	C
	⑥	25.42	35.25	3.84	0.37	PC
G8	G8	–	25.83	–	0.17	–
	①	51.47	92.5	66.67	0.16	C
	②	58.38	49.34	23.51	0.19	C
	③	40.47	11.51	14.32	0.24	PC
G9	G9	–	8.74	–	0.33	–
	①	57.54	49.34	40.60	0.19	C
	②	55.23	40.37	31.63	0.16	C

*C represents for corroded;
*UC represents for uncorroded
*PC represents for partial corroded

analyses of precipitates in Figs. 5–8 show that T_1 is the predominant phase for strengthening. Here, grains oriented to $(111)_{Al}$ exhibits the strongest corrosion susceptibility, although abundant dislocations and LAGBs (150 MPa stress-aged alloy) are introduced by stress loading in stress-added alloys or remain in the uncrystallized grains in stress-free alloys.

Furthermore, the quasi-in situ observations of 0 MPa stress-aged alloy show that IGC mainly occurs on HAGBs in grains oriented to $(111)_{Al}$ and that not all of the HAGBs were corroded. Compared to LAGBs, HAGBs possess a higher atomic disarrangement degree, which makes HAGBs easier to aggregate impurities and alloying solutes. Furthermore, preferential precipitation of continuous anodic T_1 is observed on the HAGBs (Fig. 9). Both features render HAGBs sensitive to corrosion. However, not all the HAGBs of grains oriented to $(111)_{Al}$ are corroded; some of them were partially corroded or uncorroded, as shown in Table 2. Based on the investigation of Zhang et al., the grain boundaries of a certain grain consist of continuous and discontinuous precipitates[38]. The discontinuous precipitates may hinder electrolyte penetration, thereby protecting the grains from corrosion. Electrolytes could penetrate to the subsurface through the corroded HAGBs, causing the corrosion of adjacent grain boundaries, as shown in Fig. 3a–Fig. 3b. Hence, severe localised IGC corrosion could be observed in Figs. 3 and 4. In 150 MPa stress-aged alloy, the promotion of nucleation sites in the grain interior inhibited the precipitation of T_1 on HAGBs and LAGBs; thus, the grain interior became more anodic. When the alloy is immersed in the electrolyte, active Al and Li can be dissolved from the T_1 phase. Corrosion defects appear as micro pits in the grain interior (Fig. 12d–Fig. 12h), and the electrolyte penetrates to the grain interior through the pits, leading to intragranular corrosion, which comprise the corrosion morphology in Fig. 3i.

4. Summary

(1) The major strengthening precipitates in both stress free and stress added alloy were T_1 and θ'. Their size was remarkably refined with increasing stress level. Precipitates on the grain and sub-grain boundaries were greatly suppressed because the improved precipitation of T_1 and θ' in the grain interior consumes most Cu solutes in the matrix.
(2) The number fraction of LAGBs and dislocations in the grain interior increased remarkably with increasing stress levels, but the grain size was almost unchanged.
(3) The corrosion mode evolved from local IGC to local intragranular corrosion with increasing stress levels. The number of corrosion striation in the grain interior increased in the 100 MPa stress aged alloy, and almost disappear after 150 MPa stress loading. Finely dense precipitation of T_1 leads the corrosion defects in the grain interior to pits.
(4) Corrosion preferentially occurred in the grains oriented along $(111)_{Al}$ in both stress free and stress added alloy. The precipitation of T_1 makes these grains more susceptible to corrosion than are grains with a high fraction of LAGBs and dislocations.

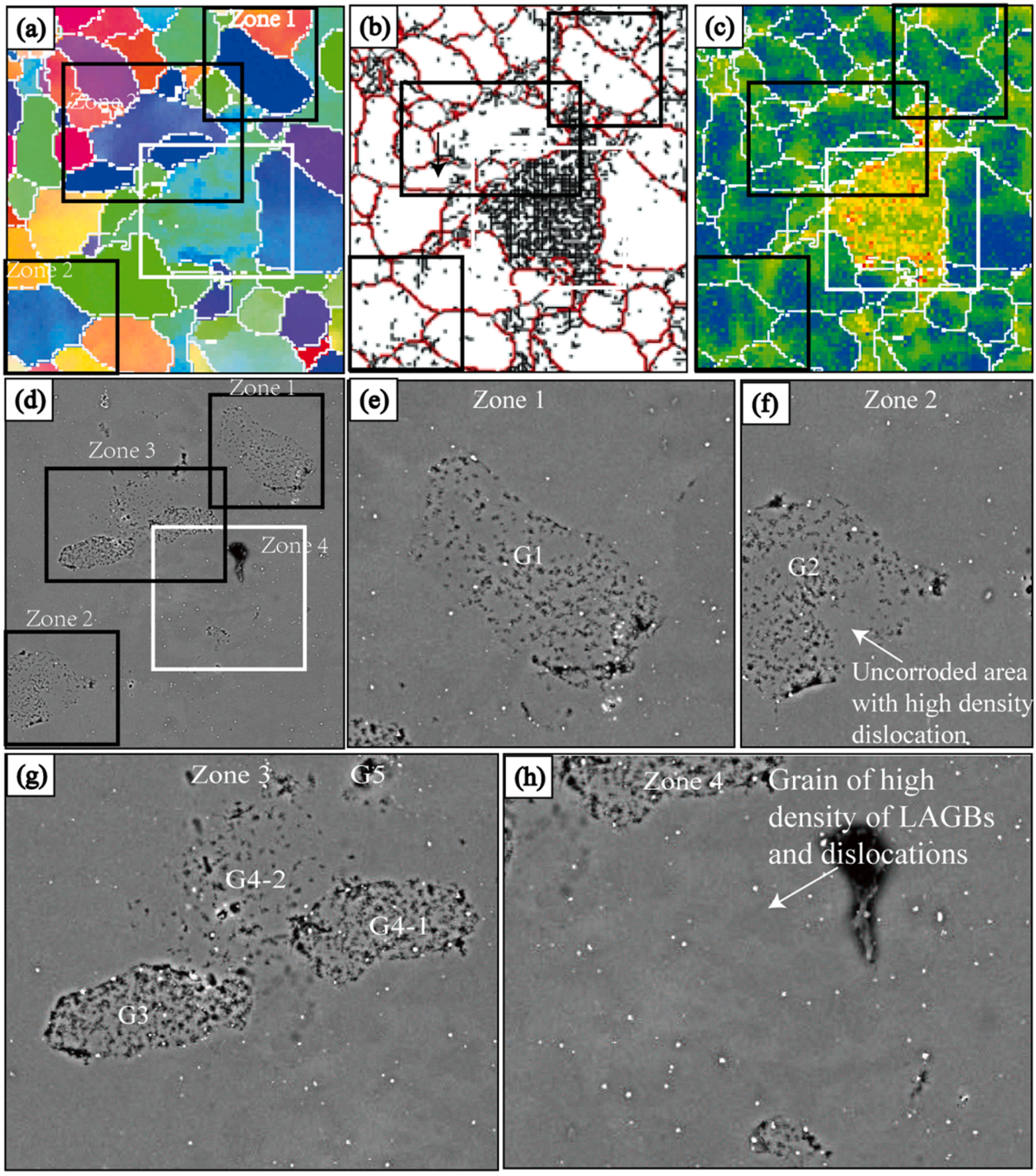

Fig. 12. EBSD (IPF-Z0) micrograph (a), grainboundaries (b) and GND (c) of creep aged Al–Cu–Li alloy (150 MPa) before immersing in 0.6 M NaCl solution for 42hrs; (d-h) were SEM micrographs of corroded defects of the EBSD observed area after immersing.

CRediT authorship contribution statement

Conceived and designed the experiments: **Bo Jiang, Shichen Li, Fuhua Cao, Danqing Yi**; Performed the experiments: **Bo Jiang, Chao Wang, Renguo Song**; Analyzed the data: **Bo Jiang, Shichen Li, Fuhua Cao**; Manuscript revision/review: **Bo Jiang, Shichen Li, Fuhua Cao**.

Declaration of Competing Interest

The authors declare that they have no known competing financial interests or personal relationships that could have appeared to influence the work reported in this paper.

Data availability

All data generated or analyzed during this study are included in this article.

Acknowledgements

The authors thank the programme of the National Natural Science Foundation of (project No.: 52001033, 12102433) and Innovation and Entrepreneurship Programme of Jiangsu Province of China (Project No. JSSCBS20210878) for financial support.

Appendix A. Supporting information

Supplementary data associated with this article can be found in the online version at doi:10.1016/j.corsci.2022.110314.

References

[1] P.D. Pitcher, C.M. Styles, Creep age forming of 2024A, 8090 and 7449 alloys, Mater. Sci. Forum 331 (2000) 455–460, https://doi.org/10.4028/www.scientific.net/msf.331-337.455.
[2] Y.L. Yang, A study of inelastic/anelastic behaviour and springback of AA7050 alloy in creep age forming, 2017.
[3] D.J. Inforzato, P.R. Costa, F.F. Fernandez, D.N. Travessa, Creep-age forming of AA7475 aluminum panels for aircraft lower wing skin application, Mater. Res. 15 (2012) 596–602, https://doi.org/10.1590/S1516-14392012005000080.
[4] L. Hu, L. Zhan, R. Shen, Z. Liu, Z. Ma, J. Liu, Y. Yang, Effects of uniaxial creep ageing on the mechanical properties and micro precipitates of Al-Li-S4 alloy, Mater. Sci. Eng. A 688 (2017) 272–279, https://doi.org/10.1016/j.msea.2017.01.081.
[5] S.S. Rui, Y.B. Shang, Y.N. Fan, Q.N. Han, L.S. Niu, H.J. Shi, K. Hashimoto, N. Komai, EBSD analysis of creep deformation induced grain lattice distortion: A new method for creep damage evaluation of austenitic stainless steels, Mater. Sci. Eng. A 733 (2018) 329–337, https://doi.org/10.1016/j.msea.2018.07.058.
[6] D. Jiang, R. Yang, D. Wang, Z. Liu, Effect of external stress on the microstructure and mechanical properties of creep-aged Al-Cu-Li-Ag alloy, Micron 143 (2021), 103011, https://doi.org/10.1016/j.micron.2021.103011.
[7] T. Ye, L. Song, Y. Liang, M. Quan, J. He, J. Lin, Precipitation behavior of ωo phase and texture evolution of a forged Ti-45Al-8.5Nb-(W, B, Y) alloy during creep, Mater. Charact. 136 (2018) 41–51, https://doi.org/10.1016/j.matchar.2017.12.007.
[8] R.J. Rioja, J. Liu, The evolution of Al-Li base products for aerospace and space applications, Metall. Mater. Trans. A: Phys. Metall. Mater. Sci. 43 (2012) 3325–3337, https://doi.org/10.1007/s11661-012-1155-z.
[9] W.A. Cassada, G.J. Shiflet, E.A. Starke, Mechanism of AI2CuLi (71), Nucleic Growth 22 (1991) 287–297.
[10] B. Decreus, A. Deschamps, F. De Geuser, P. Donnadieu, C. Sigli, M. Weyland, The influence of Cu/Li ratio on precipitation in Al-Cu-Li-x alloys, Acta Mater. 61 (2013) 2207–2218, https://doi.org/10.1016/j.actamat.2012.12.041.
[11] B.P. Huang, Z.Q. Zheng, Independent and combined roles of trace Mg and Ag additions in properties precipitation process and precipitation kinetics of Al-Cu-Li-(Mg)-(Ag)-Zr-Ti alloys, Acta Mater. 46 (1998) 4381–4393, https://doi.org/10.1016/S1359-6454(98)00079-2.
[12] G. Itoh, Q. Cui, M. Kanno, Effects of a small addition of magnesium and silver on the precipitation of T1 phase in an Al-4%Cu-1.1%Li-0.2%Zr alloy, Mater. Sci. Eng. A 211 (2002) 128–137, https://doi.org/10.1016/0921-5093(95)10157-8.
[13] D.A. Porter, K.E. Easterling, M.Y. Sherif. Phase Transformations in Metals and Alloys, Third Edition, Taylor & Francis Group, 2009.
[14] B.A. Chen, G. Liu, R.H. Wang, J.Y. Zhang, L. Jiang, J.J. Song, J. Sun, Effect of interfacial solute segregation on ductile fracture of Al – Cu – Sc alloys, Acta Mater. 61 (2013) 1676–1690, https://doi.org/10.1016/j.actamat.2012.11.043.
[15] A.W. Zhu, J. Chen, E.A. Starke, Precipitation strengthening of stress-aged Al-XCu alloys, Acta Mater. 48 (2000) 2239–2246, https://doi.org/10.1016/S1359-6454(00)00026-4.
[16] P. Ma, L. Zhan, C. Liu, J. Yang, K. Chen, Z. Huang, Strong stress-level dependence of creep-ageing behavior in Al–Cu–Li alloy, Mater. Sci. Eng. A 802 (2021), 140381, https://doi.org/10.1016/j.msea.2020.140381.
[17] J.W. Cahn, Nucleation on dislocations, Acta Metall. 5 (1957) 169–172, https://doi.org/10.1016/0001-6160(57)90021-4.
[18] J.F. Li, C.X. Li, Z.W. Peng, W.J. Chen, Z.Q. Zheng, Corrosion mechanism associated with T1 and T2 precipitates of Al-Cu-Li alloys in NaCl solution, J. Alloy. Compd. 460 (2008) 688–693, https://doi.org/10.1016/j.jallcom.2007.06.072.
[19] X. Zhang, X. Zhou, T. Hashimoto, B. Liu, C. Luo, Z. Sun, Z. Tang, F. Lu, Y. Ma, Corrosion behaviour of 2A97-T6 Al-Cu-Li alloy: the influence of non-uniform precipitation, Corros. Sci. 132 (2018) 1–8, https://doi.org/10.1016/j.corsci.2017.12.010.
[20] V. Proton, J. Alexis, E. Andrieu, J. Delfosse, A. Deschamps, F. De Geuser, M. Lafont, C. Blanc, The influence of artificial ageing on the corrosion behaviour of a 2050 aluminium – copper – lithium alloy, Corros. Sci. 80 (2014) 494–502, https://doi.org/10.1016/j.corsci.2013.11.060.
[21] N. Birbilis, R.G. Buchheit, Electrochemical characteristics of intermetallic phases in aluminum alloys: an experimental survey and discussion, J. Electrochem. Soc. 152 (2005) 140–151, https://doi.org/10.1149/1.1869984.
[22] M. Guérin, J. Alexis, E. Andrieu, L. Laffont, W. Lefebvre, G. Odemer, C. Blanc, Identification of the metallurgical parameters explaining the corrosion susceptibility in a 2050 aluminium alloy, Corros. Sci. 102 (2016) 291–300, https://doi.org/10.1016/j.corsci.2015.10.020.
[23] M. Orłowska, E. Ura-Bińczyk, L. Olejnik, M. Lewandowska, The effect of grain size and grain boundary misorientation on the corrosion resistance of commercially pure aluminium, Corros. Sci. 148 (2019) 57–70, https://doi.org/10.1016/j.corsci.2018.11.035.
[24] B. Jiang, H. Wang, Y. Tian, D. Yi, H. Liu, Z. Hu, Effects of aging time on corrosion behavior of an Al-Cu-Li alloy, Corros. Sci. 173 (2020), 108759, https://doi.org/10.1016/j.corsci.2020.108759.
[25] W.F. Hosford, S.P. Agrawal, Effect of stress during aging on the precipitation of θ′ in Al-4 Wt pct Cu, Metall. Trans. A 6 (1975) 487–491, https://doi.org/10.1007/BF02658406.
[26] J.X. Gao, Z.G. Shang, B.Q. Wei, D.D. Li, K. He, N. Yan, Absolute thickness measurement of pyrolytic graphite spheroids by STEM-EELS, Micron 91 (2016) 41–48, https://doi.org/10.1016/j.micron.2016.10.001.
[27] M. Song, W. Wang, S.P. Ringer, Y. Du, H. Shi, K. Li, J. Lu, D. Schryvers, G. Sha, H. Idrissi, Quantitative measurement for the microstructural parameters of nano-precipitates in Al-Mg-Si-Cu alloys, Mater. Charact. 118 (2016) 352–362, https://doi.org/10.1016/j.matchar.2016.06.007.
[28] D.B. William, et al.. Transmission Electron Microscopy: A Textbook for Materials Science, Second Edition, Springer, 2019.
[29] T. Dorin, A. Deschamps, F. De Geuser, W. Lefebvre, C. Sigli, Quantitative description of the T1formation kinetics in an Al-Cu-Li alloy using differential scanning calorimetry, small-angle X-ray scattering and transmission electron microscopy, Philos. Mag. 94 (2014) 1012–1030, https://doi.org/10.1080/14786435.2013.878047.
[30] J.W. Cahn, J. NuttIng, , Transmission quantitative metallography, Trans. Am. Inst. Min. Metall. Eng. 215 (1959) 526–528.
[31] M.-T.P.-P. Kassner, E. Michael. Fundamentals of Creep in Metals and Alloys, Third edit, Butterworth-Heinemann, 2004.
[32] X. Zhang, X. Zhou, J.O. Nilsson, Z. Dong, C. Cai, Corrosion behaviour of AA6082 Al-Mg-Si alloy extrusion: recrystallized and non-recrystallized structures, Corros. Sci. 144 (2018) 163–171, https://doi.org/10.1016/j.corsci.2018.08.047.
[33] X. Zhang, X. Zhou, T. Hashimoto, J. Lindsay, O. Ciuca, C. Luo, Z. Sun, X. Zhang, Z. Tang, The influence of grain structure on the corrosion behaviour of 2A97-T3 Al-Cu-Li alloy, Corros. Sci. 116 (2017) 14–21, https://doi.org/10.1016/j.corsci.2016.12.005.
[34] I. Braun, F.C. Frank, G. Meyrick, Grain boundary etching on pure aluminium, Philos. Mag. 3 (1958) 1312–1317, https://doi.org/10.1080/14786435808233314.
[35] S.H. Kim, U. Erb, K.T. Aust, G. Palumbo, Effect of texture on the corrosion behaviour of high purity aluminum, Mater. Sci. Forum 408–412 (2002) 1043–1048, https://doi.org/10.4028/www.scientific.net/msf.408-412.1043.
[36] G.M. Treacy, C.B. Breslin, Electrochemical studies on single-crystal aluminium surfaces, Electrochim. Acta 43 (1998) 1715–1720, https://doi.org/10.1016/S0013-4686(97)00305-8.
[37] P. Donnadieu, Y. Shao, F. De Geuser, G.A. Botton, S. Lazar, M. Cheynet, M. De Boissieu, A. Deschamps, Atomic structure of T1 precipitates in Al-Li-Cu alloys revisited with HAADF-STEM imaging and small-angle X-ray scattering, Acta Mater. 59 (2011) 462–472, https://doi.org/10.1016/j.actamat.2010.09.044.
[38] R. Zhang, Y. Qiu, Y. Qi, N. Birbilis, A closer inspection of a grain boundary immune to intergranular corrosion in a sensitised Al-Mg alloy, Corros. Sci. 133 (2018) 1–5, https://doi.org/10.1016/j.corsci.2018.01.009.